ARTICLES
https://doi.org/10.1038/s41560-020-00692-7

nature energy

Check for updates

Low-bandgap mixed tin–lead iodide perovskites with reduced methylammonium for simultaneous enhancement of solar cell efficiency and stability

Chongwen Li[1], Zhaoning Song[1]✉, Cong Chen[1], Chuanxiao Xiao[2], Biwas Subedi[1], Steven P. Harvey[2], Niraj Shrestha[1], Kamala Khanal Subedi[1], Lei Chen[1], Dachang Liu[1], You Li[1], Yong-Wah Kim[3], Chun-sheng Jiang[2], Michael J. Heben[1], Dewei Zhao[1], Randy J. Ellingson[1], Nikolas J. Podraza[1], Mowafak Al-Jassim[2] and Yanfa Yan[1]✉

High-performance perovskite/perovskite tandem solar cells require high-efficiency and stable low-bandgap perovskite subcells. State-of-the-art low-bandgap mixed tin–lead iodide perovskite solar cells exhibit either a high power-conversion efficiency or improved stability, but not both. Here we report a two-step bilayer interdiffusion growth process to simultaneously meet both requirements for formamidinium-based low-bandgap mixed tin–lead iodide perovskite solar cells. The bilayer interdiffusion growth process allows for the formation of high-quality and large-grained perovskite films with only 10 mol% volatile methylammonium. Additionally, one-dimensional pyrrolidinium perovskite was applied to passivate the perovskite film and improve the junction quality, which resulted in a carrier lifetime of 1.1 µs and an open circuit voltage of 0.865 V for our perovskite film and device with a bandgap of 1.28 eV. Our strategies enabled a power-conversion efficiency of 20.4% for low-bandgap perovskite solar cells under AM 1.5G illumination. More importantly, an encapsulated device can retain 92% of its initial efficiency after 450 h of continuous 1 sun illumination.

Organic–inorganic metal halide perovskite solar cells (PSCs) have reached a remarkable certified power conversion efficiency (PCE) of 25.2% (ref. [1]). Perovskite/perovskite tandem solar cells are promising to further improve the PCE and even break the Shockley–Queisser radiative limits for single-junction solar cells[2–5]. Recent advances in the low-bandgap mixed tin (Sn)–lead (Pb) iodide PSCs have enabled the fabrication of efficient perovskite/perovskite tandem solar cells in both two-terminal (2-T) and four-terminal configurations, with PCEs that reach more than 24 and 25%, respectively[6,7]. Despite the impressive progress[8–14], the current state-of-the-art mixed Sn–Pb PSCs exhibit an important shortcoming: they are either efficient or stable, but not both.

The high-efficiency PSCs typically use formamidinium/methylammonium (FA/MA)-based mixed Sn–Pb perovskite absorbers with a high MA proportion (≥30 mol%) (refs. [15–20]). The high MA proportion leads to large perovskite grains that are critical to realize high PCEs[21–23]. However, including a high proportion of volatile MA cations makes the devices unstable against heat and light stresses[24–28]. Alternatively, MA-free FA/caesium (Cs)-based mixed Sn–Pb perovskite absorbers exhibit a high device stability under illumination. Recently, a stable operation of PSCs based on $FA_{0.75}Cs_{0.25}Sn_{0.4}Pb_{0.6}I_3$ absorbers for up to 1,000 h was demonstrated[10]. For the FA/Cs-based mixed Sn–Pb PSCs, Cs was used to stabilize the perovskite phase, which boosted the performance and stability[5]. However, the incorporation of a substantial amount of Cs accelerates the perovskite crystallization process, which leads to small grain sizes and a substantial number of grain boundaries, which compromise the PCE of the resultant PSCs[29,30]. A viable way to overcome this dilemma is to synthesize high-quality FA-based mixed Sn–Pb perovskite films with large grains but a low MA proportion. However, the current fabrication processes of mixed Sn–Pb PSCs are incapable of realizing the aforementioned goal.

The most commonly used process to fabricate a high PCE mixed Sn–Pb PSCs is one-step antisolvent-assisted spin coating[17]. This process has been advanced recently by the achievements with high-efficiency PSCs. For instance, the incorporation of a small dose of cadmium ions into $FA_{0.5}MA_{0.45}Cs_{0.05}Pb_{0.5}Sn_{0.5}I_3$ demonstrated an enhanced electron diffusion length, which enabled mixed Sn–Pb PSCs with a PCE of about 20.0% (ref. [9]). Moreover, a strategy that used metallic tin to suppress Sn^{2+} oxidation via a comproportionation process has been developed. The single-junction $FA_{0.7}MA_{0.3}Pb_{0.5}Sn_{0.5}I_3$ PSCs that utilize the Sn reduction strategy have delivered a PCE of 21.1%, which enabled the fabrication of perovskite/perovskite tandem solar cells with a PCE of 24.8% (ref. [6]). Despite the recent progress, this one-step deposition method has its limitation in preparing high-quality large-grained mixed Sn–Pb perovskite films in which the MA proportion is below 30 mol% (ref. [17]).

Here we report a two-step bilayer interdiffusion growth (BIG) strategy to successfully reduce the MA proportion to 10% without compromising grain size and device performance. We further applied pyrrolidinium thiocyanate (PySCN) to form the one-dimensional (1D) $PySn_xPb_{1-x}I_3$ perovskite which passivates the film surface and grain boundaries[31,32]. As a result, the carrier lifetime of thick mixed Sn-Pb perovskite films increased to 1.1 µs, which is essential for an efficient photoexcited charge carrier collection in a thick absorber layer[7]. The incorporation of PySCN also

[1]Department of Physics and Astronomy and Wright Center for Photovoltaics Innovation and Commercialization, The University of Toledo, Toledo, OH, USA. [2]Materials Science Center, National Renewable Energy Laboratory, Golden, CO, USA. [3]Department of Chemistry and Biochemistry, The University of Toledo, Toledo, OH, USA. ✉e-mail: zhaoning.song@utoledo.edu; yanfa.yan@utoledo.edu

improves the junction quality at the perovskite/electron transport layer (ETL) interface, which boosts the open circuit voltage (V_{OC}) to 0.865 V. Our champion device based on the FA-based mixed Sn–Pb perovskite absorbers delivers a PCE of 20.4% (20.3%) measured under a reverse (forward) voltage scan, which is comparable with the best FA/MA-based mixed Sn–Pb PSCs[6,7]. Benefiting from the reduced MA content and improved perovskite film quality, our mixed Sn–Pb PSCs show excellent stability against light and heat. An encapsulated mixed Sn–Pb PSC retained 92% of its initial efficiency after 450 h of continuous operation under one sun illumination.

BIG of FA-based Sn–Pb perovskites

The two-step sequential deposition technique is widely used to fabricate high-efficiency pure-Pb PSCs due to its simple and precise process control as well as its good reproducibility[33]. However, no success has been realized in mixed Sn–Pb perovskites with a Sn ratio of ~50% due to the rapid crystallization of Sn-based perovskites[34]. We first tested the synthesis of mixed Sn–Pb perovskite films via the conventional two-step method[33]. On spin coating the formamidinium iodide (FAI)/methylammonium chloride (MACl) in isopropyl alcohol (IPA) solution on a predeposited tin(II) iodide (SnI_2)/lead iodide (PbI_2) film, the film turned black rapidly, which is due to the stronger reaction of Sn^{2+} than that of Pb^{2+} with FAI[34]. The rapid formation of small-sized perovskite grains blocks the diffusion of the organic halide salts, which results in organic residues on the surface and unreacted SnI_2/PbI_2 at the bottom after annealing (Supplementary Fig. 1). The excess organic impurities cause excessive non-radiative recombination, whereas the unreacted SnI_2/PbI_2 hinders charge transport, which limit the device performance (Supplementary Fig. 2)[35].

To overcome the above issues, we designed the two-step BIG process with a prolonged ion diffusion and exchange stage to enable the full conversion of SnI_2/PbI_2 into the perovskite phase, which allows for an increased grain size of mixed Sn–Pb perovskites with a low MA concentration. Figure 1a illustrates the process flow diagram of our BIG process. We employed additional methylammonium thiocyanate (MASCN) (25 mol%) in the first-step SnI_2/PbI_2 precursor solution to promote the formation of mixed Sn–Pb perovskite nanocrystallites that help suppress the preferential rapid reaction between SnI_2 and FAI in the next step. MASCN was selected because SCN ions exhibit a stronger bonding with Sn ions than that of halogen ions and can help suppress the oxidization of Sn^{2+} (ref. [34]). The SnI_2/PbI_2/MASCN precursor solution was first spin coated on a substrate, and an FAI/IPA solution was subsequently spin coated to form a bilayer precursor film. An interdiffusion stage at a low temperature of 50 °C was applied to promote the diffusion of FA ions and exchange of FA/MA cations, which allowed the coalescence of the bilayer and completed the conversion of precursors to the perovskite phase. This stage also enabled a final annealing temperature of 120 °C, which provides sufficient thermal energy to promote grain growth and eliminate organic residues.

We tracked and analysed the evolution of the crystal phase and microstructure of the mixed Sn–Pb perovskite films during the BIG process by X-ray diffraction (XRD) and scanning electron microscopy (SEM) measurements (Fig. 1b–i). The XRD pattern of a spin-coated SnI_2/PbI_2/MASCN precursor film shows a small peak at ~14.15° (Fig. 1b), which corresponds to the (110) plane of $MASn_{0.5}Pb_{0.5}I_3$ (ref. [36]). The low peak intensity indicates that $MASn_{0.5}Pb_{0.5}I_3$ perovskite nanocrystallites have already formed in the as-prepared precursor film. The existence of solvents prevented their further growth. After a FAI/IPA solution was spin coated onto the SnI_2/PbI_2/MASCN precursor film, the XRD peak of the (110) plane shifted to a lower angle of ~14° with a slightly increased peak intensity (Fig. 1c), which indicates that that FA cations reacted with metal halides and started to form the FA-based perovskites. The top-view SEM image in Fig. 1d shows that small (average size of 300–500 nm) but distinct grains were formed during this early stage, which correlates with the stronger XRD peak intensity. The corresponding cross-sectional SEM image (Fig. 1g) further reveals that the grains were formed in a bilayer structure that consisted of an upper layer of FA-based perovskite and a lower perovskite layer, which contained unreacted SnI_2/PbI_2/MASCN precursor complexes. A 50 °C annealing stage was then applied to promote FA diffusion and FA/MA ion exchange. The XRD pattern of a 50 °C annealed film (Fig. 1b) shows no obvious changes in the peak intensity or location, which indicates the lack of sufficient thermal energy to promote grain growth. The top-view SEM image of this stage (Fig. 1e) shows the coalescence of grains, which results in a more uniform and smoother surface compared with that of the as-prepared film (Fig. 1d). The cross-sectional SEM (Fig. 1h) shows that the bilayer grains merged into a monolayer, which indicates the interdiffusion/ion exchange between the upper FA-based perovskite layer and the lower precursor complex layer[21]. The final annealing at a relatively high temperature of 120 °C dramatically increased the diffraction peak intensity in the XRD pattern (Fig. 1b), which indicates an enhanced grain size and crystallinity of the film. Additionally, the (110) peak shifted slightly towards a lower angle (13.98°), which is attributed to further MA/FA ion exchange promoted by the higher thermal energy. No SnI_2/PbI_2 residual peak was detected by XRD, which confirms the complete conversion of SnI_2/PbI_2 into the perovskite phase. The high-temperature annealing promoted grain growth to an average size of over 1 μm (Fig. 1f) and eliminated horizontal grain boundaries (Fig. 1i).

The diffusion stage at 50 °C is critical to the synthesis of high-quality thick mixed Sn–Pb perovskite films. We first explored the annealing of the as-prepared film directly at 120 °C and found a layer of unreacted SnI_2/PbI_2 at the bottom of the perovskite layer (Supplementary Fig. 3). The metal iodide residues impeded the extraction at the interface between the mixed Sn–Pb perovskite absorber layer and the poly(3,4-ethylenedioxythiophene):polystyrene sulfonate (PEDOT:PSS) hole-transport layer (HTL), which limited the performance of the resultant PSCs (Supplementary Fig. 4). The incomplete perovskite conversion is probably due to the fast evaporation of solvent at a high temperature, which causes insufficient diffusion of FAI into the layer underneath. Thus, a diffusion stage at a mild temperature is needed to ensure a sufficient ion exchange. However, the diffusion stage cannot be too long because a longer duration (for example, 7 or 15 min) enlarges the grain size of the perovskite (Supplementary Fig. 5a–d), but severely deteriorates the crystallinity and grain integrity of the final perovskite films, which show eroded and porous grains (Supplementary Fig. 5e–h). The XRD measurements (Supplementary Fig. 6) of the films with longer diffusion-stage durations show lower peak intensities than that of the film annealed for three minutes, which corresponds to a decreased crystallinity and undesirable film morphology.

The degradation caused by long-duration diffusion is attributed to the dynamic change of solvents in the film at this stage. We used temperature-programmed desorption mass spectrometry (TPD-MS) to track the volatile species released from the 50 °C annealed perovskite film. We observed a high partial pressure of IPA at a relatively low temperature of ~50 °C and the release of dimethylformamide (DMF) and dimethylsulfoxide (DMSO) at a higher temperature (~60 °C), along with the vaporization of excess FA in the form of its derivative fragments (Supplementary Fig. 7). Therefore, if the duration of pre-annealing at 50 °C exceeds its proper processing window, IPA will evaporate and the remaining DMF/DMSO will re-dissolve and erode the perovskite during the diffusion stage. Also, the result shows that if the diffusion-stage temperature exceeds 60 °C, a faster evaporation of DMSO, DMF and FA gases will lead to incomplete conversion, as in the case of direct high-temperature annealing (Supplementary Fig. 6). Therefore, the

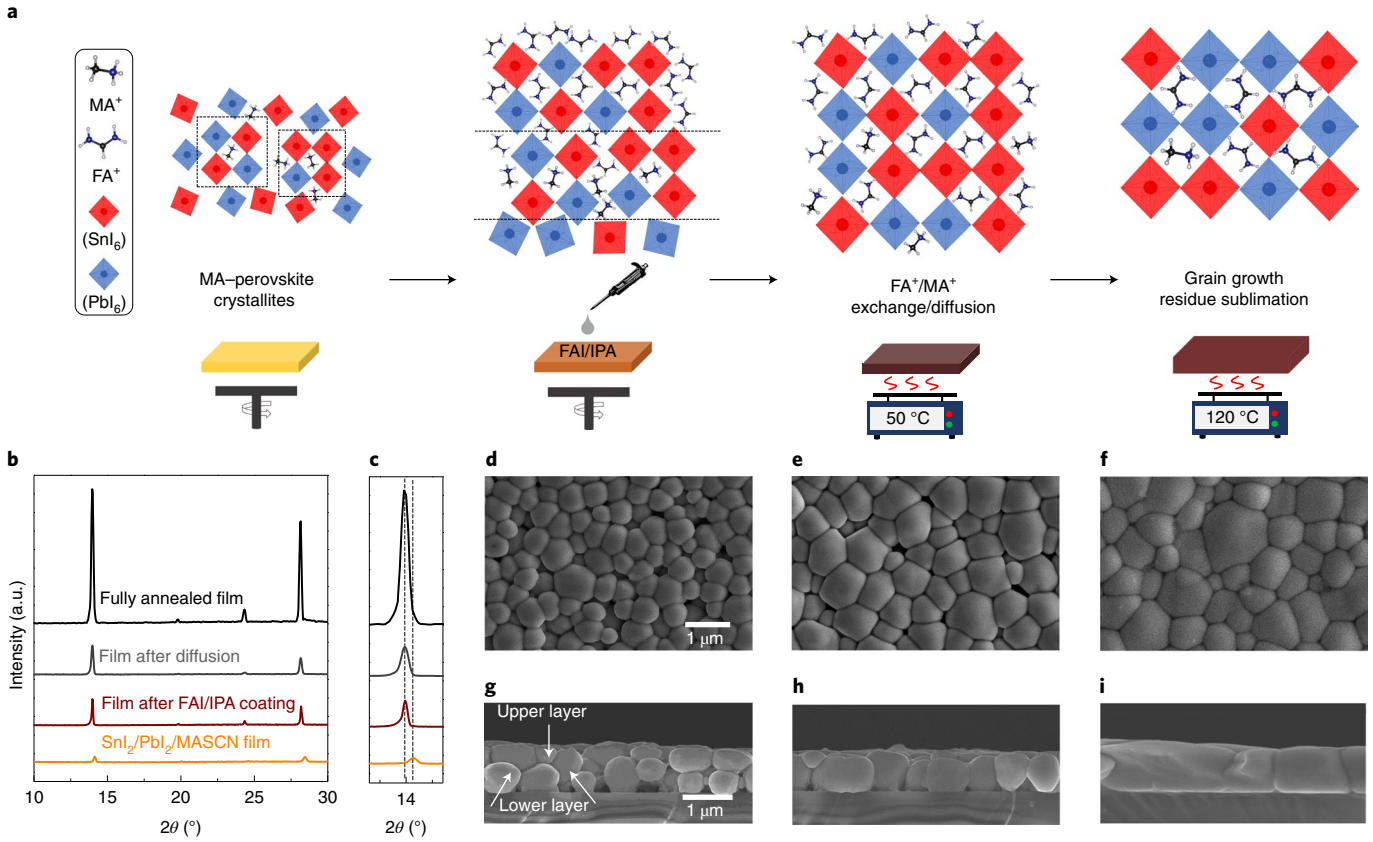

Fig. 1 | Mixed Sn–Pb perovskite films prepared by the BIG process. a, Schematic diagram of the BIG process. **b**,**c**, XRD patterns of films at each processing stage (**b**) and the expanded figure at around 14° of 2θ (**c**). The dashed lines indicate the evolution of the characteristic peak that corresponds to the (110) plane. **d**–**i**, Top-view (**d**–**f**) and cross-sectional (**g**–**i**) SEM images of the perovskite films after FAI/IPA coating (**d** and **g**), the diffusion stage (**e** and **h**) and final annealing (**f** and **i**). The scale is the same for all images. a.u., arbitrary units.

optimal duration (about three minutes) and pre-annealing temperature (50 °C) are desirable for the diffusion stage of the BIG process, which leads to high-quality mixed Sn–Pb perovskite films.

The thickness of mixed Sn–Pb perovskite films is determined by the concentration of the SnI_2/PbI_2 precursor solution. The perovskite film thickness increases from 600 ± 55 to 960 ± 91 nm by changing the concentration of the SnI_2/PbI_2/MASCN precursor solution from 1.4 to 1.7 M (Supplementary Figs. 8 and 9). For the mixed Sn–Pb perovskite, although a thicker absorber layer is preferred to ensure sufficient light absorption[3,9,18], the sub-bandgap defect state density increases with increases in the bulk volume of the film, as evident from the increasing Urbach energy measured by photothermal deflection spectroscopy (PDS) (Supplementary Fig. 9). These sub-bandgap defect states cause charge recombination, which shortens the carrier lifetime and so lowers the V_{OC} and fill factor (FF) for the thicker mixed Sn–Pb PSCs (Supplementary Fig. 10). To balance the trade-off between increasing photon absorption and avoiding defect formation, an optimal thickness of 900 ± 69 nm by using the 1.6 M precursor solution was selected. The mixed Sn–Pb perovskite film prepared by the BIG method showed a carrier lifetime of 565 ns and an Urbach energy of 26.7 ± 1 meV, which are comparable to those of the single-step processed $(FASnI_3)_{0.6}(MAPbI_3)_{0.4}$ perovskite films (Supplementary Fig. 11). The long carrier lifetime and low defect density are desired for high-performance PSCs[7].

To evaluate the photovoltaic performance of the mixed Sn–Pb perovskite films prepared by the BIG process, we utilized this method to fabricate PSCs with a p–i–n configuration of glass/indium tin oxide (ITO)/PEDOT:PSS/perovskite/fullerene (C_{60})/bathocuproine (BCP)/Ag. It is known that the addition of alkali cations, such as Cs^+ and Rb^+, is beneficial to the device performance because the cations can increase entropy, modify the tolerance factor and reduce lattice strains[12,37–40]. Here, 5 mol% caesium iodide (CsI) was incorporated to improve the reproducibility and eliminate the hysteresis in current density–voltage (J–V) measurements (Supplementary Fig. 12) of the mixed Sn–Pb PSCs without changing the chemical phase and microstructure of the perovskite thin films (Supplementary Fig. 13). The bandgap of the Cs-containing mixed Sn–Pb film measured by spectroscopic ellipsometry (SE) is 1.28 eV (Supplementary Fig. 14), which is consistent with that of other mixed Sn–Pb perovskites with a Sn/Pb atomic ratio of 1:1 reported in the literature[41,42]. We fabricated 30 PSCs using the BIG-processed mixed Sn–Pb perovskite absorber layers, and the statistics of the photovoltaic parameters are summarized in Supplementary Table 1 and Supplementary Fig. 15. The average PCEs of the PSCs that contained 5 mol% CsI are 18.91 ± 0.36% (18.86 ± 0.35%) under a reverse (forward) voltage scan, which shows negligible J–V hysteresis (Supplementary Fig. 12).

Impact of MA concentration on film thermal stability

^{1}H NMR spectroscopy was used to quantitatively analyse the molar ratio of FA/MA in the BIG-processed mixed Sn–Pb perovskite films. We made several perovskite films using the BIG process and scraped the perovskite powders from the substrates. The perovskite powders were then dissolved in DMSO-d_6 for the ^{1}H NMR measurement, and the spectrum is shown in Supplementary Fig. 16. The histogram analysis of the normalized NMR peak intensities that correspond to individual chemical species is shown in Fig. 2a, from which the composition of our BIG-processed mixed Sn–Pb perovskite is estimated to be about $FA_{0.85}MA_{0.1}Cs_{0.05}Sn_{0.5}Pb_{0.5}I_3$.

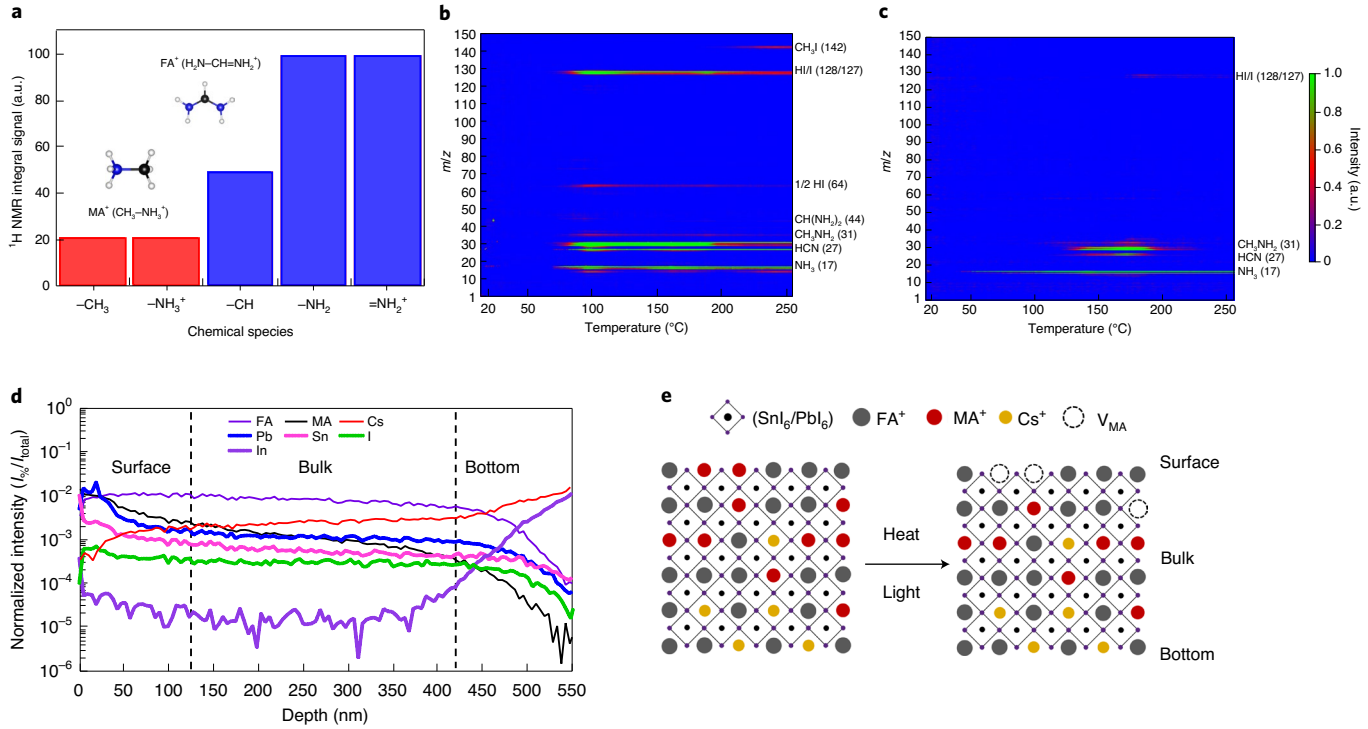

Fig. 2 | Composition and degradation of mixed Sn–Pb perovskite films fabricated by the BIG process. a, ^{1}H NMR analysis of mixed Sn–Pb perovskites prepared by the BIG process. **b**,**c**, TPD-MS of $(FASnI_3)_{0.6}(MAPbI_3)_{0.4}$ (**b**) and $FA_{0.85}MA_{0.1}Cs_{0.05}Sn_{0.5}Pb_{0.5}I_3$ (**c**) perovskite films. **d**, TOF-SIMS depth profile of a $FA_{0.85}MA_{0.1}Cs_{0.05}Sn_{0.5}Pb_{0.5}I_3$ perovskite film made by the BIG process and deposited over a glass substrate. The normalized intensity is on a logarithmic scale. **e**, Schematic diagram of the elemental distribution in the $FA_{0.85}MA_{0.1}Cs_{0.05}Sn_{0.5}Pb_{0.5}I_3$ film and surface degradation due to heat and light stresses (V_{MA} represents MA vacancies).

We then performed TPD-MS measurements to compare the thermal stability of a BIG-processed $FA_{0.85}MA_{0.1}Cs_{0.05}Sn_{0.5}Pb_{0.5}I_3$ perovskite film with a $(FASnI_3)_{0.6}(MAPbI_3)_{0.4}$ film prepared by the one-step method. The $(FASnI_3)_{0.6}(MAPbI_3)_{0.4}$ film released MA (CH_3NH_2) and hydroiodic acid (HI) gas species at a low temperature of ~68 °C and became more pronounced with increasing temperature, which indicates the commencement of thermal decomposition at ~68 °C (Fig. 2b). In contrast, the $FA_{0.85}MA_{0.1}Cs_{0.05}Sn_{0.5}Pb_{0.5}I_3$ film prepared by the BIG method showed a much improved thermal stability, with MA and FA fragments released at ~125 °C (Fig. 2c and Supplementary Fig. 17). Interestingly, the release of the HI signal starts later than that of the organic species at ~170 °C, which indicates the lower MA content makes the mixed Sn–Pb perovskite more thermally stable. We then performed a more thorough thermal stability study of various mixed Sn–Pb films and confirmed that reducing the MA content is, indeed, beneficial for the stability of mixed Sn–Pb perovskite films (Supplementary Figs. 18 and 19).

A time-of-flight secondary ion mass spectroscopy (TOF–SIMS) measurement was performed to probe the depth profile of a $FA_{0.85}MA_{0.1}Cs_{0.05}Sn_{0.5}Pb_{0.5}I_3$ perovskite film. As shown in Fig. 2d, the signals that correspond to Sn^{2+}, Pb^{2+}, I^- and FA^+ are almost constant throughout the film thickness, which indicates the uniform distribution of these elements. Interestingly, the MA^+ signal shows a decreasing gradient from the film surface (0 nm) to the perovskite/ITO glass interface, whereas the signal of Cs^+ shows a positive gradient. Although the unusual increased signal intensity in the surface region (~50 nm) could be due to the degradation during sample shipment or to ion-beam damage[43], the trends of MA^+ and Cs^+ are complementary in the bulk of the perovskite. The higher concentration of Cs^+ at the bottom may be due to the lower diffusion coefficient of Cs^+ than that of MA^+. The component distribution indicates the MA concentration is relatively higher in the surface region than in the film bulk region, as illustrated in Fig. 2e. The MA ions in the surface are easier to decompose by heat and light stresses, which is in good agreement with the short release period of MA species (Fig. 2c and Supplementary Fig. 20). The formed MA and I vacancies lead to the formation of recombination centres, which degrade the PSC performance[44–46]. Therefore, a strategy to passivate the top surface of BIG-processed mixed Sn–Pb perovskite films is needed.

Surface passivation using 1D pyrrolidine perovskite

We introduced the 1D $PySn_xPb_{1-x}I_3$ perovskite to passivate the surface and grain boundaries of our BIG-processed $FA_{0.85}MA_{0.1}Cs_{0.05}Sn_{0.5}Pb_{0.5}I_3$ perovskite films. The impact of the PySCN proportion on the chemical phase and microstructure of mixed Sn–Pb perovskites was studied (Supplementary Figs. 21 and 22)[31]. When the PySCN proportion was increased to 5 mol%, the grain size reduced and pinholes and voids between grains formed (Supplementary Fig. 22d). The voids cause undesirable recombination, which adversely affects the device performance. Incorporation of an optimal proportion (1.5 mol%) of PySCN enhanced the photoluminescence (PL) emission and increases the mean carrier lifetime from 670 ns to 1.1 µs (Fig. 3a and Supplementary Fig. 23). The microsecond lifetime is comparable with the lifetime of high-quality FA/MA-based mixed Sn–Pb perovskites[7]. The prolonged carrier lifetime is attributed to the grain-boundary passivation by 1D $PySn_xPb_{1-x}I_3$ perovskites. The surface potential mapping shows a more pronounced upward potential bending at the grain boundaries of the mixed Sn–Pb film after the addition of PySCN (Supplementary Fig. 24), which indicates a stronger electron attraction and hole repulsion at grain boundaries, known as a feature of defect passivation[47].

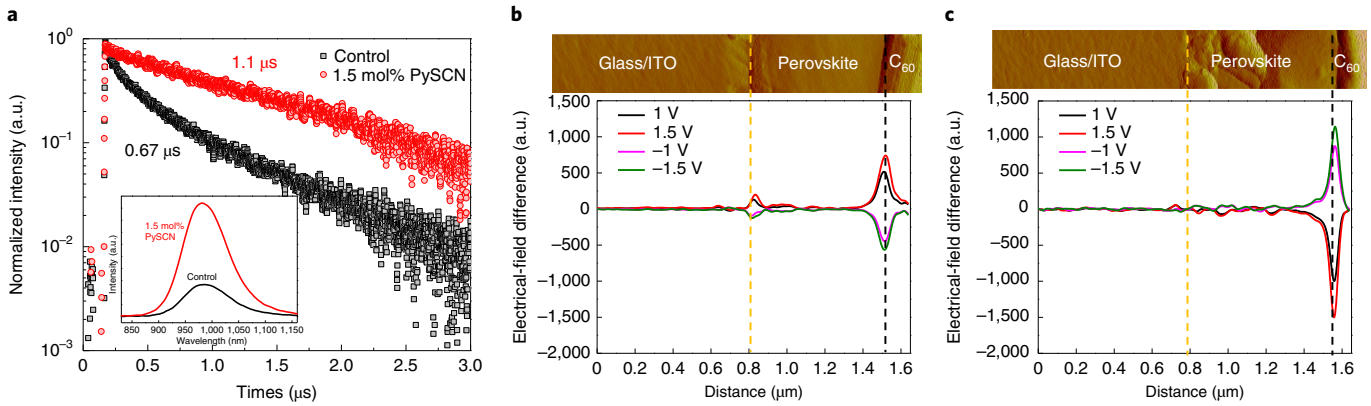

Fig. 3 | 1D $PySn_xPb_{1-x}I_3$ passivation of mixed Sn–Pb perovskite thin films. a, Time-resolved photoluminescence (TRPL) decays and PL spectra (inset) of the $FA_{0.85}MA_{0.1}Cs_{0.05}Sn_{0.5}Pb_{0.5}I_3$ perovskite films without (control) and with 1.5 mol% PySCN. **b**,**c**, Cross-sectional KPFM potential maps and the corresponding electric field profiles of the $FA_{0.85}MA_{0.1}Cs_{0.05}Sn_{0.5}Pb_{0.5}I_3$ films without (**b**) and with (**c**) 1.5 mol% PySCN. The dashed lines indicate the interfaces of ITO/perovskite (yellow) and perovskite/C_{60} (black). The four potential difference curves were obtained by subtracting the 0 V profile curve from the potential profiles measured under different bias voltages from −1.5 to 1 V.

The formation of 1D $PySn_xPb_{1-x}I_3$ perovskites on the surface of mixed Sn–Pb perovskite absorber layers also favourably influences junction quality, as revealed by cross-sectional Kelvin probe force microscopy (KPFM) measurements. The potential line profiles, potential differences with respect to the zero bias and electrical-field difference are shown in Supplementary Fig. 25 and Fig. 3b,c. Without the PySCN incorporation, a small peak is seen at the HTL/perovskite junction in the profiles of the electrical-field differences measured with various bias, besides the main peak at the perovskite/ETL junction (Fig. 3b). However, with 1.5 mol% PySCN incorporation, the peak at the HTL/perovskite junction disappeared to leave only the peak at the perovskite/ETL junction (Fig. 3c). This behaviour is clear evidence of improved junctions, as we demonstrated previously in various perovskite device configurations[48–50]. This positive effect on junction quality and enhanced carrier lifetime led to an improved V_{OC} and FF when a small amount of PySCN was incorporated. The V_{OC} reached a maximum when the incorporation of PySCN reached 1.5 mol% (Supplementary Fig. 26).

Performance and stability of single-junction and tandem PSCs

We fabricated single-junction mixed Sn–Pb PSCs using the 1.5 mol%-PySCN-incorporated $FA_{0.85}MA_{0.1}Cs_{0.05}Sn_{0.5}Pb_{0.5}I_3$ perovskites as the absorber layers. Figure 4a shows the histogram of the PCEs of 30 cells. The detailed photovoltaic parameters of the PCSs are shown in Supplementary Fig. 27 and Supplementary Table 2, and show good reproducibility and negligible *J*–*V* hysteresis. Noticeable improvements in V_{OC} and FF due to the $PySn_xPb_{1-x}I_3$ passivation were observed. Figure 4b shows the *J*–*V* curves of the best-performing device measured under reverse and forward voltage scans. The cell delivered a PCE of 20.4 (20.3)%, a V_{OC} of 0.865 (0.864) V, a short circuit current (J_{SC}) of 29.81 (29.85) mA–cm^{-2} and a FF of 79.1 (78.7)% under the reverse (forward) voltage scan. The J_{SC} values match well with the integrated photocurrent density of 29.33 mA cm^{-2} deduced from the external quantum efficiency (EQE) spectrum (Fig. 4c). More importantly, the FA-based mixed Sn–Pb PSCs show decent operational stability. As shown in Fig. 4g, an encapsulated $FA_{0.85}MA_{0.1}Cs_{0.05}Sn_{0.5}Pb_{0.5}I_3$ cell retained 92% of its original efficiency after maximum power point (MPP) tracking for 450 h under continuous one sun illumination. This robust operational stability is mainly attributed to the BIG-processed FA-based mixed Sn–Pb perovskite after comparing devices with different compositions and passivation (Supplementary Figs. 28 and 29). Moreover, we performed an accelerated thermal degradation test of mixed Sn–Pb PSCs following the perovskite community consensus[47]. We found that the BIG-processed $FA_{0.85}MA_{0.1}Cs_{0.05}Sn_{0.5}Pb_{0.5}I_3$ PSCs demonstrated a considerably improved intrinsic thermal stability compared with that of the conventional $(FASnI_3)_{0.6}(MAPbI_3)_{0.4}$ when aged at 85 °C in nitrogen (Supplementary Fig. 30). It has been found that the thermal stability of most mixed Sn–Pb PSCs is limited by the use of acidic PEDOT:PSS and corrosive Ag electrode[14]. The real-world applications of mixed Sn–Pb PSCs require more stable HTLs, electrodes and encapsulation techniques.

The stable low-bandgap FA-based mixed Sn–Pb PSCs enabled us to fabricate stable 2-T perovskite/perovskite tandem solar cells. The tandem cells, which consisted of 1.73 eV wide-bandgap top subcells and 1.28 eV BIG-processed low-bandgap bottom subcells were fabricated following a procedure reported previously[19]. The device architecture is depicted in Supplementary Fig. 31, and the corresponding cross-sectional SEM image is shown in Fig. 4d. Benefiting from the high-quality mixed Sn–Pb subcell prepared by the BIG process with the $PySn_xPb_{1-x}I_3$ passivation, the champion tandem cell exhibited a PCE of 23.3% (23.3%), with a high V_{OC} of 1.943 (1.937) V, J_{SC} of 15.1 (15.2) mA cm^{-2} and FF of 79.3% (79%) under the reverse (forward) voltage scan (Fig. 4e). The integrated J_{SC} values for wide- and low-bandgap subcells calculated from the EQE spectra (Fig. 4f) were 15.0 and 14.8 mA cm^{-2}, respectively, which are consistent with the J_{SC} value from the *J*–*V* curves. The stable low-bandgap mixed Sn–Pb subcells enabled the stable operation of our perovskite/perovskite tandem solar cells. Figure 4g illustrates that an encapsulated 2-T perovskite/perovskite tandem solar cell retained 85% of its initial PCE after MMP tracking for more than 350 h under 1 sun illumination, which is remarkably improved compared with the device that used the conventional mixed Sn–Pb subcell (Supplementary Fig. 32).

Conclusions

In summary, we developed a two-step BIG process to fabricate high-efficiency and high-stability FA-based mixed Sn–Pb PSCs. The deposition process was systematically investigated to understand the perovskite formation mechanism. The mixed Sn–Pb absorber films exhibited large grains and a low MA concentration. Single-junction PSCs using the $FA_{0.85}MA_{0.1}Cs_{0.05}Sn_{0.5}Pb_{0.5}I_3$ absorber layers prepared by the BIG process achieved a best PCE of 20.4% and demonstrated

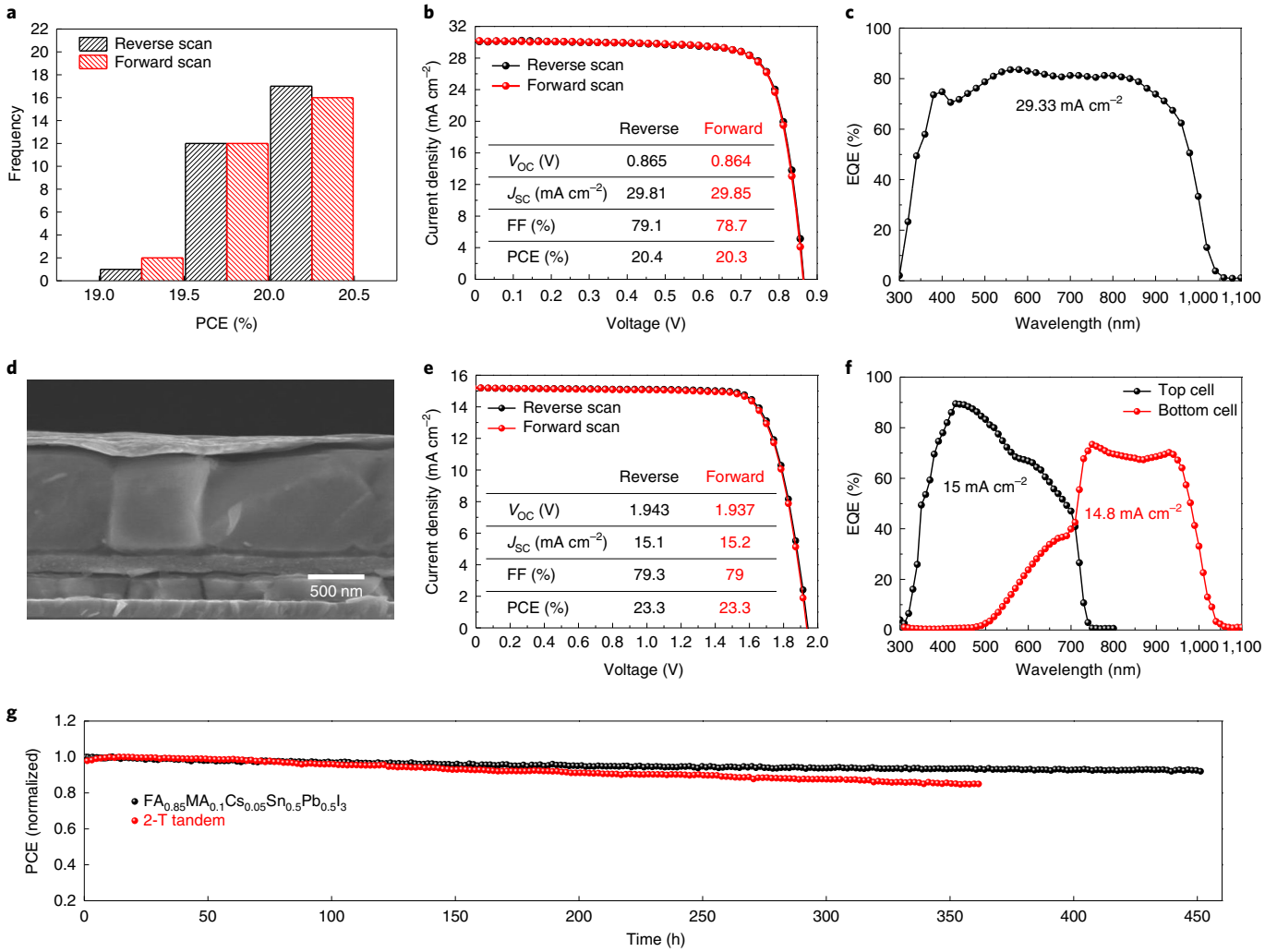

Fig. 4 | Single-junction and tandem PSCs. a, Histogram of the PCEs for 30 $FA_{0.85}MA_{0.1}Cs_{0.05}Sn_{0.5}Pb_{0.5}I_3$ mixed Sn–Pb PSCs with 1.5 mol% PySCN. **b**,**c**, *J*–*V* curves (**b**) and EQE spectrum (**c**) of the best-performing single-junction mixed Sn–Pb PSC. The integrated J_{SC} from the EQE curve is 29.33 mA cm^{-2}, as marked in the figure. **d**, Cross-sectional SEM image of a perovskite/perovskite tandem solar cell. **e**,**f**, *J*–*V* curves (**e**) and EQE spectrum (**f**) of the best-performing perovskite/perovskite tandem solar cell. The integrated J_{SC} values from the EQE data of wide- and low-bandgap subcells are 15 and 14.8 mA cm^{-2}, respectively. **g**, MPP tracking of a $FA_{0.85}MA_{0.1}Cs_{0.05}Sn_{0.5}Pb_{0.5}I_3$ PSC and a 2-T perovskite/perovskite tandem cell with encapsulation measured in the air under simulated AM 1.5G solar illumination. The initial PCEs for the single-junction $FA_{0.85}MA_{0.1}Cs_{0.05}Sn_{0.5}Pb_{0.5}I_3$ PSC and the 2-T tandem cell were 19.8 and 23.1%, respectively.

MPP stability for more than 450 h of continuous operation with a power loss of less than 10%. The stable low-bandgap mixed Sn–Pb PSCs enabled the fabrication of 2-T perovskite/perovskite tandem cells with PCEs that exceeded 23%. A tandem cell retained 85% of its initial PCE after 350 h of continuous operation under MPP tracking. Our BIG process paves a pathway to simultaneously maximize performance and stability for mixed Sn–Pb PSCs. However, further improvements in the design of the device architecture and selection of materials are needed to enable a better PCE and stability of tandem cells.

Methods

Materials. SnI_2, lead thiocyanate, MACl, diethyl ether, tin(II) fluoride, DMF and IPA were purchased from Aldrich Sigma. PbI_2 and CsI were purchased from Alfa Aesar. FAI, methylammonium iodide, MASCN and PySCN were purchased from GreatCell Solar. Poly(triaryl amine) was purchased from Xi'an Polymer Light Technology Corp. PEDOT:PSS was purchased from Heraeus company. 2,3,5,6-Tetrafuoro-7,7,8,8-tetracyanoquinodimethane and BCP were purchased from Jilin OLED Company. The ITO target and silver were purchased from Kurt J. Lesker.

One-step $(FASnI_3)_{0.6}(MAPbI_3)_{0.4}$ low-bandgap perovskite precursor. The precursor solution was prepared by the same recipe reported in our previous work. SnI_2 (372 mg), FAI (172 mg) and tin(II) fluoride (15.6 mg) were dissolved in a mixed solvent of DMF (424 µl) and DMSO (212 µl) to prepare the $FASnI_3$ precursor solution. PbI_2 (461 mg), methylammonium iodide (159 mg) and lead thiocyanate (11.3 mg) were dissolved in a mixed solvent of DMF (633 µl) and DMSO (71 µl). The two solutions were then mixed at the molar ratio of 6:4 to form the $(FASnI_3)_{0.6}(MAPbI_3)_{0.4}$ precursor solution.

Two-step conventional mixed Sn–Pb low-bandgap perovskite precursor. PbI_2 (345.8 mg) and SnI_2 (279.5 mg) were dissolved in a mixed solvent of DMF (900 µl) and DMSO (100 µl) to form the first-step precursor solution. FAI (60 mg) and MACI (6 mg) were dissolved in IPA (1 µl) to form the second-step precursor.

Two-step BIG-processed $FA_{0.85}MA_{0.1}Cs_{0.05}Sn_{0.5}Pb_{0.5}I_3$ perovskite precursor. PbI_2 (230.5 mg), SnI_2 (186.3 mg), CsI (12.99 mg) and MASCN (22.54 mg) were dissolved in a DMF and DMSO mixed solvent for the $FA_{0.85}MA_{0.1}Cs_{0.05}Sn_{0.5}Pb_{0.5}I_3$ precursor. CsI was removed from the recipe to prepare the FA-based mixed Sn–Pb perovskite without Cs^+, with everything else kept the same. To change the precursor solution concentration, mixed DMF/DMSO solvents of 714/51, 667/47, 625/44 and 588/42 µl were used to prepare the 1.4, 1.5, 1.6 and 1.7 M precursor

solution, respectively. An additional 1.3, 2.0 and 6.5 mg of PySCN were added to the precursor to form the 1, 1.5 and 5 mol%, respectively, $PySn_xPb_{1-x}I_3$ passivation. FAI (60 mg) were dissolved in 1 µl of IPA to form the second-step precursor.

$FA_{0.8}Cs_{0.2}Pb(I_{0.7}Br_{0.3})_3$ wide-bandgap perovskite precursor. FAI (126.6 mg), CsI (47.8 mg), $PbBr_2$ (152.0 mg) and PbI_2 (233.2 mg) were dissolved in the mixed solvent of 750 µl of DMF and 250 µl of DMSO.

One-step $(FASnI_3)_{0.6}(MAPbI_3)_{0.4}$ low-bandgap PSC fabrication. The HTL PEDOT:PSS was spin coated on the ITO substrate at 4,000 r.p.m. for 50 s, followed by a 150 °C annealing for 15 min. The perovskite solution (40 µl) was spin coated onto the PEDOT:PSS layer at 5,000 r.p.m. for 60 s. Diethyl ether was applied dropwise onto the film 5 s from the start of the spin. The film was then transferred to a 100 °C hotplate for 7 min. After cooling to room temperature, the film was kept in a sealed box and then transferred to a Kurt J. Lesker thermal evaporation system. C_{60} (20 nm), BCP (5 nm) and Ag (80 nm) were sequentially evaporated on the perovskite film to form a PSC device. Unless otherwise mentioned, the HTL-, ETL- and electrode-fabrication processes were the same for other low-bandgap PSCs.

Two-step conventional mixed Sn–Pb low-bandgap PSC fabrication. A SnI_2/PbI_2 (40 µl) precursor solution was spin coated on PEDOT:PSS at 1,500 r.p.m. for 30 s, followed by a 70 °C annealing for 2 min. After spinning, 150 µl of FAI/MACl solution was dropped on the precursor film and the excess solution was spin dried immediately by another 1,500 r.p.m. spin for 30 s. The film was then annealed on a 100 °C hotplate before it was transferred to the evaporation system to fabricate the ETL and electrode.

Two-step BIG-processed $FA_{0.85}MA_{0.1}Cs_{0.05}Sn_{0.5}Pb_{0.5}I_3$ PSC fabrication. The first-step precursor solution SnI_2/PbI_2/MASCN/CsI/PySCN (40 µl) was spin coated on the PEDOT:PSS substrate at 1,500 r.p.m. for 30 s. Then, 200 µl of the second-step FAI precursor solution was dropped on the precursor film followed by an immediate spin of 1,500 r.p.m for another 30 s. The delay between applying FAI and the second-step spinning needed to be finished within 1 s. The film was then transferred to a 50 °C hotplate for 3 min for the diffusion of FAI and full transformation of the perovskite phase. Afterwards, the film was transferred to a 120 °C hotplate for 7 min for further grain growth. The annealed film was then sealed and transferred to the evaporation system to fabricate the ETL and electrode.

2-T perovskite/perovskite tandem solar cell fabrication. Poly(triaryl amine) solution (80 µl) was spin coated on the ITO substrate at 4,000 r.p.m. for 30 s and then the substrate was annealed at 100 °C for 10 min. DMF (70 µl) was spin coated at 4,000 r.p.m. for 10 s to improve the wettability of the poly(triaryl amine) surface prior to wide-bandgap perovskite deposition. The perovskite precursor was spin coated at 500 r.p.m. for 3 s and then at 4,000 r.p.m. for 60 s. During the 4,000 r.p.m. step, 750 µl of diethyl ether was applied dropwise in the centre of the substrate to facilitate the crystallization. After that, the substrate was annealed at 60 °C for 2 min and at 100 °C for 5 min. Next, the substrate was transferred to the vacuum chamber. C_{60} (20 nm) and BCP (5 nm) were thermally evaporated sequentially. The substrate was then transferred to the radio-frequency magnetron sputtering system. A 130 nm ITO layer was sputtered from the 76.2 mm ITO target (In_2O_3/SnO_2 90/10 wt%; Lesker) at a 70 W power under an Ar pressure of 2 mtorr. Then, PEDOT:PSS diluted with IPA (volume ratio 1:1) was spin coated on the sputtering ITO layer, followed by 5 min of annealing on a 100 °C hotplate in air. After annealing, the film was immediately transferred to a glove box for the BIG-processed $FA_{0.85}MA_{0.1}Cs_{0.05}Sn_{0.5}Pb_{0.5}I_3$ layer deposition, which followed the same process as discussed above. Finally, the film was transferred in a sealed box to the thermal evaporation system to evaporate the ETL and electrode.

XRD. A Rigaku Ultima III XRD with Cu Kα radiation was used to measure and analyse the crystal structure and properties of the one-step processed and conventionally processed low-bandgap mixed Sn–Pb perovskites, the $FA_{0.85}MA_{0.1}Cs_{0.05}Sn_{0.5}Pb_{0.5}I_3$ precursor films at each stage during the BIG process, as well as the films with different concentrations of PySCN passivation.

SEM. A high-resolution field-emission Hitachi S-4800 SEM was used to measure the top-view and cross-sectional images of the conventional processed low-bandgap mixed Sn–Pb perovskites and the $FA_{0.85}MA_{0.1}Cs_{0.05}Sn_{0.5}Pb_{0.5}I_3$ precursor films at each stage during the BIG process, as well as the films with different concentrations of PySCN passivation.

KPFM. Scanning KPFM measurements were performed in an Ar-filled glove box using a Vecco D5000 atomic force microscope. A PPP-EFM tip was operated in tapping mode for the cross-sectional potential distribution. The electrical resolution was ~10 mV. In the junction measurement, we cleaved the solar cell to expose the cross-sectional surface; the ITO was grounded and various bias voltages were applied to the Ag side. No polishing or ion-milling treatment was introduced to the sample preparation to avoid artefacts.

PDS measurement. PDS measurements were collected using a custom system (PTS-3-PTD, Sciencetech Inc.) operated in transverse configuration[51] over a spectral range of 1,400–800 nm (0.89–1.55 eV) in 10 nm steps. The monochromatic pump beam was modulated with a mechanical chopper at 0.2 Hz. The probe beam was a 633 nm laser of a nominally 300 µm cross-sectional diameter. Perovskite films were placed into a quartz cuvette, which was then filled with Fluorinert (C_6F_{14} fluid) while inside a nitrogen-purged glove box. PDS measurements were collected for perovskite films without exposure to the atmosphere. The Urbach energy of perovskite films was calculated by the linear fitting of the corresponding PDS curve. The Urbach energy was determined by the inverse of the slope of a linear fit to $\ln(\alpha/\alpha_g)$ below bandgap, where α is the absorption coefficient spectra and α_g is the absorption coefficient at the bandgap energy. The standard error in the slope was scaled with the square root of a reduced chi-squared statistic (the linear fit; Origin 2020).

^{1}H NMR spectroscopy. The proton spectra were acquired on a Bruker Avance III NMR spectrometer with a DCH Cryoprobe at 600 MHz. The data were collected at 22 °C using a one-pulse sequence with a 30° flip pulse of 3.3 µs, acquisition time of 2.7 s. and a recycle delay of 1 s.

TPD-MS. The TPD-MS measurements were performed using a built-in-house TPD system. The mass spectra in a range of 1 to 150 atomic mass units were recorded by a quadrupole mass spectrometer (Stanford Research System, RGA 300) using a custom LabVIEW program, following a previously reported procedure. For a typical TPD routine, the furnace temperature was ramped up from room temperature to 500 °C at a ramp rate of 1.67 °C min^{-1}.

TOF–SIMS. An ION-TOF TOF-SIMS V spectrometer was used for depth profiling and chemical imaging of the perovskite. Analysis was completed using a three-lens 30 kV BiMn primary-ion gun. 1D profiles were completed utilizing the Bi^{3+} primary-ion beam (0.8 pA pulsed beam current) and a 50 × 50 µm area was analysed with a 128:128 primary beam raster. Sputtering for surface cleaning and depth profiling was accomplished with 1 kV oxygen and caesium ion sputter beams (~5 nA sputter current for each source) with a raster of 200 × 200 µm. After completion of the SIMS measurements, the depth of the SIMS sputter craters was determined by optical interference light microscopy to convert the SIMS sputter timescale to a sputter depth scale.

TRPL. TRPL measurements were conducted using a time-correlated single-photon counting module (Becker & Hickel Simple Tau SPCM 130-E/M module). Samples were excited by a 532 nm pulsed laser (~5 ps pulse width, ~150 µm spot diameter; Fianium model SC400-2) at ~10^{10} photons pulse^{-1} cm^{-2}. Radiative recombination events were detected via an InP/InGaAsP near-infrared photomultiplier tube detector (Hamamatsu H10330A-45) after dispersion by an iHR-320 monochromator grating (900 g mm^{-1}, 850 nm blaze). PL decay curves were biexponential in nature and fitted by iterative reconvolution with the measured system response function. The mean photogenerated carrier lifetime for the biexponential fit was calculated by the weighted-average method.

SE and unpolarized transmittance measurement. Immediately following PDS measurement, each film was removed from the C_6F_{14} fluid into the laboratory ambient for SE and unpolarized transmittance measurements. Both measurements were collected using a multichannel rotating-compensator spectroscopic ellipsometer (M-2000FI, J. A. Woollam Co., Inc.) over a spectral range of 1676–210 nm (0.74–5.89 eV). The SE and unpolarized transmittance measurements were collected at a 70° and 0° angle of incidence, respectively, with the SE being measured in terms of $N = \cos(2\psi)$, $C = \sin(2\psi)\cos\Delta$ and $S = \sin(2\psi)\sin\Delta$, where ψ is the amplitude ratio and Δ is the phase difference between *p*- and *s*-polarized light waves, respectively, N, C and S are the non-zero elements of the isotropic Mueller matrix. The combined time for sample mounting, alignment and data acquisition for these two measurements, that is the length of time the films were in the laboratory ambient air, was approximately 2–3 min.

PSC characterization. The PSCs were encapsulated with cover glasses and then sealed by ultraviolet-curable epoxy before conducting the *J*–*V* measurements, MMP tracking measurements and EQE measurements in the ambient air. *J*–*V* curves were measured under 100 mW cm^{-2} AM 1.5G solar irradiation (PV Measurements Inc.) with a Keithley 2400 Source Meter.

The light intensity for the *J*–*V* measurements was calibrated by a standard silicon wafer solar cell and the PSCs certified by Newport. The MMP tracking measurements for both the $FA_{0.85}MA_{0.1}Cs_{0.05}Sn_{0.5}Pb_{0.5}I_3$ single-junction PSC and the fabricated 2-T tandem cell were conducted in air under a full-spectrum one sun illumination without any light filter. The humidity of the measurement environment ranged from 40 to 60%. Especially, the single-junction $FA_{0.85}MA_{0.1}Cs_{0.05}Sn_{0.5}Pb_{0.5}I_3$ PSC was tracked under room temperature, whereas for the 2-T tandem cells the environment temperature was kept at 25 °C to limit the water and oxygen ingression through the encapsulant from the humid measurement environment. A 0.1 cm^2 area mask was used to define the active area of a PSC. A quantum efficiency system (model IVQE8-C, PV Measurements

Inc.) was used to measure the quantum efficiency of the PSCs. A standard silicon wafer solar cell was used as the reference for the EQE measurement. We used bias illumination to measure the EQE for the 2-T tandem cell. The EQEs of the top and bottom subcells were measured by exposing the 2-T tandem cell under 530 and 940 nm LED lamps, respectively, to saturate the other junction during EQE measurement. The thermal stability tests were conducted by ageing the PEDOT:PSS-free devices on a hotplate at 85 °C in a nitrogen glove box. The devices were then encapsulated and periodically taken out to the ambient air for *J*–*V* measurements. Once the measurement of a device was done, the device was placed back on the hotplate in the glove box immediately to prevent the inevitable leakage and oxidization.

Reporting Summary. Further information on research design is available in the Nature Research Reporting Summary linked to this article.

Data availability

All data generated or analysed during this study are included in the published article and its Supplementary Information.

Received: 26 December 2019; Accepted: 21 August 2020;
Published online: 15 October 2020

References

1. *Best Research-Cell Efficiency Chart* https://www.nrel.gov/pv/cell-efficiency.html (NREL, accessed 25 March 2020).
2. Shockley, W. & Queisser, H. J. Detailed balance limit of efficiency of p–n junction solar cells. *J. Appl. Phys.* **32**, 510–519 (1961).
3. Hörantner, M. T. et al. The potential of multijunction perovskite solar cells. *ACS Energy Lett.* **2**, 2506–2513 (2017).
4. Leijtens, T., Bush, K. A., Prasanna, R. & McGehee, M. D. Opportunities and challenges for tandem solar cells using metal halide perovskite semiconductors. *Nat. Energy* **3**, 828–838 (2018).
5. Eperon, G. E. et al. Perovskite–perovskite tandem photovoltaics with optimized band gaps. *Science* **354**, 861–865 (2016).
6. Lin, R. et al. Monolithic all-perovskite tandem solar cells with 24.8% efficiency exploiting comproportionation to suppress Sn(II) oxidation in precursor ink. *Nat. Energy* **4**, 864–873 (2019).
7. Tong, J. et al. Carrier lifetimes of >1 μs in Sn–Pb perovskites enable efficient all-perovskite tandem solar cells. *Science* **364**, 475–479 (2019).
8. Chen, B., Zheng, X., Bai, Y., Padture, N. P. & Huang, J. Progress in tandem solar cells based on hybrid organic–inorganic perovskites. *Adv. Energy Mater.* **7**, 1602400 (2017).
9. Yang, Z. et al. Enhancing electron diffusion length in narrow-bandgap perovskites for efficient monolithic perovskite tandem solar cells. *Nat. Commun.* **10**, 4498 (2019).
10. Prasanna, R. et al. Design of low bandgap tin–lead halide perovskite solar cells to achieve thermal, atmospheric and operational stability. *Nat. Energy* **4**, 939–947 (2019).
11. Leijtens, T. et al. Tin–lead halide perovskites with improved thermal and air stability for efficient all-perovskite tandem solar cells. *Sustain. Energy Fuels* **2**, 2450–2459 (2018).
12. Kapil, G. et al. Strain relaxation and light management in tin–lead perovskite solar cells to achieve high efficiencies. *ACS Energy Lett.* **4**, 1991–1998 (2019).
13. Forgács, D. et al. Efficient monolithic perovskite/perovskite tandem solar cells. *Adv. Energy Mater.* **7**, 1602121 (2017).
14. Wei, M. et al. Combining efficiency and stability in mixed tin–lead perovskite solar cells by capping grains with an ultrathin 2*d* layer. *Adv. Mater.* **32**, 1907058 (2020).
15. Wang, C., Song, Z., Li, C., Zhao, D. & Yan, Y. Low-bandgap mixed tin–lead perovskites and their applications in all-perovskite tandem solar cells. *Adv. Funct. Mater.* **29**, 1808801 (2019).
16. Xu, G. et al. Integrating ultrathin bulk–heterojunction organic semiconductor intermediary for high-performance low-bandgap perovskite solar cells with low energy loss. *Adv. Funct. Mater.* **28**, 1804427 (2018).
17. Liao, W. et al. Fabrication of efficient low-bandgap perovskite solar cells by combining formamidinium tin iodide with methylammonium lead iodide. *J. Am. Chem. Soc.* **138**, 12360–12363 (2016).
18. Zhao, D. et al. Low-bandgap mixed tin–lead iodide perovskite absorbers with long carrier lifetimes for all-perovskite tandem solar cells. *Nat. Energy* **2**, 17018 (2017).
19. Zhao, D. et al. Efficient two-terminal all-perovskite tandem solar cells enabled by high-quality low-bandgap absorber layers. *Nat. Energy* **3**, 1093–1100 (2018).
20. Li, C. et al. Reducing saturation-current density to realize high-efficiency low-bandgap mixed tin–lead halide perovskite solar cells. *Adv. Energy Mater.* **9**, 1803135 (2019).
21. Li, C. et al. Methylammonium-mediated evolution of mixed-organic-cation perovskite thin films: a dynamic composition-tuning process. *Angew. Chem.* **56**, 7674–7678 (2017).
22. Tang, S. et al. Composition engineering in doctor-blading of perovskite solar cells. *Adv. Energy Mater.* **7**, 1700302 (2017).
23. Yang, M. et al. Perovskite ink with wide processing window for scalable high-efficiency solar cells. *Nat. Energy* **2**, 17038 (2017).
24. Song, Z. et al. Probing the origins of photodegradation in organic–inorganic metal halide perovskites with time-resolved mass spectrometry. *Sustain. Energy Fuels* **2**, 2460–2467 (2018).
25. Lang, F. et al. Influence of radiation on the properties and the stability of hybrid perovskites. *Adv. Mater.* **30**, 1702905 (2018).
26. Turren-Cruz, S.-H., Hagfeldt, A. & Saliba, M. Methylammonium-free, high-performance, and stable perovskite solar cells on a planar architecture. *Science* **362**, 449–453 (2018).
27. Juarez-Perez, E. J. et al. Photodecomposition and thermal decomposition in methylammonium halide lead perovskites and inferred design principles to increase photovoltaic device stability. *J. Mater. Chem. A* **6**, 9604–9612 (2018).
28. Juarez-Perez, E. J., Ono, L. K. & Qi, Y. Thermal degradation of formamidinium based lead halide perovskites into *sym*-triazine and hydrogen cyanide observed by coupled thermogravimetry–mass spectrometry analysis. *J. Mater. Chem. A* **7**, 16912–16919 (2019).
29. Prasanna, R. et al. Band gap tuning via lattice contraction and octahedral tilting in perovskite materials for photovoltaics. *J. Am. Chem. Soc.* **139**, 11117–11124 (2017).
30. Yu, Y. et al. Improving the performance of formamidinium and cesium lead triiodide perovskite solar cells using lead thiocyanate additives. *ChemSusChem* **9**, 3288–3297 (2016).
31. Xu, A. F. et al. Pyrrolidinium lead iodide from crystallography: a new perovskite with low bandgap and good water resistance. *Chem. Commun.* **55**, 3251–3253 (2019).
32. Fan, J. et al. Thermodynamically self-healing 1*d*–3*d* hybrid perovskite solar cells. *Adv. Energy Mater.* **8**, 1703421 (2018).
33. Jiang, Q. et al. Surface passivation of perovskite film for efficient solar cells. *Nat. Photon.* **13**, 460–466 (2019).
34. Lian, X. et al. Highly efficient Sn/Pb binary perovskite solar cell via precursor engineering: a two-step fabrication process. *Adv. Funct. Mater.* **29**, 1807024 (2019).
35. Jacobsson, T. J. et al. Unreacted PbI_2 as a double-edged sword for enhancing the performance of perovskite solar cells. *J. Am. Chem. Soc.* **138**, 10331–10343 (2016).
36. Ogomi, Y. et al. $CH_3NH_3Sn_xPb_{(1-x)}I_3$ perovskite solar cells covering up to 1060 nm. *J. Phys. Chem. Lett.* **5**, 1004–1011 (2014).
37. Saliba, M. et al. Incorporation of rubidium cations into perovskite solar cells improves photovoltaic performance. *Science* **354**, 206–209 (2016).
38. Lee, J.-W. et al. Formamidinium and cesium hybridization for photo- and moisture-stable perovskite solar cell. *Adv. Energy Mater.* **5**, 1501310 (2015).
39. Yi, C. et al. Entropic stabilization of mixed A-cation ABX_3 metal halide perovskites for high performance perovskite solar cells. *Energy Environ. Sci.* **9**, 656–662 (2016).
40. Saliba, M. et al. Cesium-containing triple cation perovskite solar cells: improved stability, reproducibility and high efficiency. *Energy Environ. Sci.* **9**, 1989–1997 (2016).
41. Im, J., Stoumpos, C. C., Jin, H., Freeman, A. J. & Kanatzidis, M. G. Antagonism between spin–orbit coupling and steric effects causes anomalous band gap evolution in the perovskite photovoltaic materials $CH_3NH_3Sn_{1-x}Pb_xI_3$. *J. Phys. Chem. Lett.* **6**, 3503–3509 (2015).
42. Hao, F., Stoumpos, C. C., Chang, R. P. & Kanatzidis, M. G. Anomalous band gap behavior in mixed Sn and Pb perovskites enables broadening of absorption spectrum in solar cells. *J. Am. Chem. Soc.* **136**, 8094–8099 (2014).
43. Harvey, S. P. et al. Mitigating measurement artifacts in TOF–SIMS analysis of perovskite solar cells. *ACS Appl. Mater. Interfaces* **11**, 30911–30918 (2019).
44. Chen, B., Rudd, P. N., Yang, S., Yuan, Y. & Huang, J. Imperfections and their passivation in halide perovskite solar cells. *Chem. Soc. Rev.* **48**, 3842–3867 (2019).
45. Yang, W. S. et al. Iodide management in formamidinium–lead–halide-based perovskite layers for efficient solar cells. *Science* **356**, 1376–1379 (2017).
46. Yin, W.-J., Shi, T. & Yan, Y. Unusual defect physics in $CH_3NH_3PbI_3$ perovskite solar cell absorber. *Appl. Phys. Lett.* **104**, 063903 (2014).
47. Khenkin, M. V. et al. Consensus statement for stability assessment and reporting for perovskite photovoltaics based on ISOS procedures. *Nat. Energy* **5**, 35–49 (2020).
48. Wang, C. et al. Understanding and eliminating hysteresis for highly efficient planar perovskite solar cells. *Adv. Energy Mater.* **7**, 1700414 (2017).
49. Chen, C. et al. Achieving a high open-circuit voltage in inverted wide-bandgap perovskite solar cells with a graded perovskite homojunction. *Nano Energy* **61**, 141–147 (2019).
50. Xiao, C. et al. Inhomogeneous doping of perovskite materials by dopants from hole-transport layer. *Matter* **2**, 1–12 (2019).
51. Jackson, W. B., Amer, N. M., Boccara, A. C. & Fournier, D. Photothermal deflection spectroscopy and detection. *Appl. Opt.* **20**, 1333–1344 (1981).

Acknowledgements

This material is based on work supported by the US Department of Energy's Office of Energy Efficiency and Renewable Energy (EERE) under the Solar Energy Technologies Office Award no. DE-EE0008753. The TPD-MS study was supported by the National Science Foundation under contract no. DMR-1807818. K.K.S. and R.J.E. were supported by the US Air Force Research Laboratory under agreement no. FA9453-18-2-0037, and N.S., B.S., N.J.P. and R.J.E. were supported by the US Air Force Research Laboratory under agreement no. FA9453-19-C-1002. The US Government is authorized to reproduce and distribute reprints for Governmental purposes notwithstanding any copyright notation thereon.

Author contributions

C.L., Z.S. and Y.Y. conceived the project. C.L. carried out the single-junction low-bandgap cell and tandem cell fabrication. C.C. prepared the wide-bandgap cell and helped with the tandem cell fabrication. D.L. participated in the wide-bandgap cell fabrication. Z.S. conducted the TPD-MS measurements. C.X. and C.J. helped with the KPFM. B.S. conducted the PDS and SE measurement. S.P.H. conducted the TOF–SIMS measurement. N.S. and K.K.S. helped with the PL and TRPL measurements. L.C. and Y.L. participated in the characterization. Y.-W.K. helped with the ^{1}H NMR measurements. C.L., Z.S. and Y.Y. analysed the data and wrote the manuscript. M.J.H., D.Z., RJ.E., N.J.P. and M.A.-J. helped with the manuscript preparation. All the authors discussed the results and commented on the manuscript. Y.Y. supervised the project.

Competing interests

The authors declare no competing interests.

Additional information

Supplementary information is available for this paper at https://doi.org/10.1038/s41560-020-00692-7.

Correspondence and requests for materials should be addressed to Z.S. or Y.Y.

Reprints and permissions information is available at www.nature.com/reprints.

Publisher's note Springer Nature remains neutral with regard to jurisdictional claims in published maps and institutional affiliations.

nature research

Corresponding author(s): Yanfa Yan and Zhaoning Song

Solar Cells Reporting Summary

Nature Research wishes to improve the reproducibility of the work that we publish. This form is intended for publication with all accepted papers reporting the characterization of photovoltaic devices and provides structure for consistency and transparency in reporting. Some list items might not apply to an individual manuscript, but all fields must be completed for clarity.

For further information on Nature Research policies, including our data availability policy, see Authors & Referees.

Experimental design

Please check: are the following details reported in the manuscript?

1. Dimensions			
Area of the tested solar cells	☒ Yes ☐ No	0.12 cm2	
Method used to determine the device area	☒ Yes ☐ No	The device area is defined by the overlap area between the ITO pattern and the shadow mask for the metal electrode.	
2. Current-voltage characterization			
Current density-voltage (J-V) plots in both forward and backward direction	☒ Yes ☐ No	Forward and reverse voltage scans.	
Voltage scan conditions *For instance: scan direction, speed, dwell times*	☒ Yes ☐ No	Forward and reverse voltage scans. The scan speed for single-junction cells is 130 mV/s. The scan speed for 2-T tandem cells is 200 mV/s.	
Test environment *For instance: characterization temperature, in air or in glove box*	☒ Yes ☐ No	J-V measurement for both single-junction and 2-T tandem cells were conducted in ambient air and at room temperature.	
Protocol for preconditioning of the device before its characterization	☐ Yes ☒ No	No preconditioning was applied before characterizations.	
Stability of the J-V characteristic *Verified with time evolution of the maximum power point or with the photocurrent at maximum power point; see ref. 7 for details.*	☒ Yes ☐ No	Figure 4g, supplementary Figure 28, 29, 30 and 32.	
3. Hysteresis or any other unusual behaviour			
Description of the unusual behaviour observed during the characterization	☒ Yes ☐ No	Negligible hysteresis was observed.	
Related experimental data	☒ Yes ☐ No	Figure 4b and e, Supplementary Figure 12.	
4. Efficiency			
External quantum efficiency (EQE) or incident photons to current efficiency (IPCE)	☒ Yes ☐ No	Figure 4c and f.	
A comparison between the integrated response under the standard reference spectrum and the response measure under the simulator	☒ Yes ☐ No	Figure 4b and c, Figure 4e and f.	
For tandem solar cells, the bias illumination and bias voltage used for each subcell	☒ Yes ☐ No	We used bias illumination to measure the EQE for 2-T tandem cells. The EQE of top and bottom sub-cells were measured by respectively exposing the 2-T tandem cell under a 530 nm and 940 nm LED lamp for saturating the other junction during measurement.	
5. Calibration			
Light source and reference cell or sensor used for the characterization	☒ Yes ☐ No	The light intensity for J–V measurements was calibrated by a standard silicon wafer solar cell certified by Newport. A standard silicon wafer solar cell was used as the reference for the EQE measurement. The description can be found in the Method.	

Confirmation that the reference cell was calibrated and certified	☒ Yes ☐ No	The light intensity for J–V measurements was calibrated by a standard silicon wafer solar cell certified by Newport. A standard silicon wafer solar cell was used as the reference for the EQE measurement.
Calculation of spectral mismatch between the reference cell and the devices under test	☒ Yes ☐ No	There is spectral mismatch between our simulator and the AM1.5 G spectrum. The simulated solar spectrum is slightly higher than the reference in the wavelength range of 500 to 700 nm and slightly lower than the reference in the wavelength range of 700 to 1100nm. Overall, the uncertainty of estimated tandem JSC for tandem cells was ~4%, and was underestimated by the slightly underestimated JSC of the low-bandgap mixed Sn-Pb subcell.

6. Mask/aperture

Size of the mask/aperture used during testing	☒ Yes ☐ No	0.1 cm2
Variation of the measured short-circuit current density with the mask/aperture area	☐ Yes ☒ No	We measured the short-circuit current density with an identical mask.

7. Performance certification

Identity of the independent certification laboratory that confirmed the photovoltaic performance	☐ Yes ☒ No	We calibrated our solar simulator by a standard silicon wafer solar cell and a Newport certified low-bandgap PSC made by our group before (Nature Energy (2) 17018 (2017)).
A copy of any certificate(s) *Provide in Supplementary Information*	☐ Yes ☒ No	We don't have a certification.

8. Statistics

Number of solar cells tested	☒ Yes ☐ No	Figure 4a caption, Supplementary Figure 2 caption, Supplementary Figure 4 caption, Supplementary Figure 10 caption, Supplementary Figure 15 caption, Supplementary Figure 17 caption.
Statistical analysis of the device performance	☒ Yes ☐ No	Discussion of Figure 4a, Supplementary Figure 2, 4, 10, 15 and 17.

9. Long-term stability analysis

Type of analysis, bias conditions and environmental conditions *For instance: illumination type, temperature, atmosphere humidity, encapsulation method, preconditioning temperature*	☒ Yes ☐ No	Methods, Figure 4g, supplementary Figure 28, 29, 30 and 32.